A Variable-Bandwidth Low-Pass Filter Approach-based Power Sharing and Voltage Regulation in Hybrid Energy Storage Systems for DC Microgrid Applications

Siddhartha Bomma, and Udaya Bhasker Manthati, *Member, IEEE*

***Abstract*—In DC microgrids, battery–supercapacitor-based hybrid energy storage systems (HESSs) are widely adopted to compensate for power imbalances between distributed generation and load variations. Conventional control methods exhibit limited capability in accurately diverting high-frequency components within the Supercapacitor (SC) current loop. To overcome this limitation, this paper proposes a variable-bandwidth scheduling strategy aimed at improving the SC current tracking performance in HESS. Unlike traditional designs, the proposed approach removes the constant low-pass filter from the SC current loop and varies the bandwidth of the current decomposition process within the HESS. This paper propose a variable bandwidth filter for diverting the currents for battery and SC based on voltage of SC. By applying different bandwidths for a low pass filter based on the SC voltage, the DC-link voltage ripple is decreased, and the SC utilization is optimized within the HESS. Consequently, the error signal to the battery is diverted to be given to the SC current. Furthermore, the controller gains are appropriately tuned to ensure stable system response based on the classical Bode analysis of the resultant transfer function. The effectiveness of the proposed current diversion is verified through simulation and experimental results.**

Link to graphical and video abstracts, and to code: https://latamt.ieeer9.org/index.php/transactions/article/view/10806

***Index Terms*—Battery, SC, Variable bandwidth filter, PI Control, DC microgrid.**

I. Introduction

In recent decades, DC microgrids (MGs), and Electric vehicles (EVs) have gained increased attention due to the depletion of fossil fuel resources and heightened environmental concerns [1]. DC microgrids enable the efficient integration of renewable energy sources (RESs), energy storage systems (ESSs), and power electronic loads, thereby improving system sustainability and energy management [2]. Although battery-based ESSs offer high energy density, their dynamic response to rapid charge–discharge transients is limited. To overcome this limitation, hybrid energy storage systems (HESSs), combining batteries with supercapacitors (SCs), are employed to satisfy power demand fluctuations and enhance overall system stability. Photovoltaic (PV) power plants inherently possess limited operational flexibility due to the intermittent nature of the primary energy source, in contrast to conventional generation units [3]. This variability increases the complexity of power system operation, as additional mechanisms are required to maintain the balance between generation and demand. To mitigate these challenges, large-scale PV plants in several countries have recently been permitted to participate in ancillary service markets by exploiting the controllability and fast response capabilities of power electronic converter interfaces [4].

The incorporation of energy storage systems (ESSs) significantly enhances the ability of PV plants to support grid services, thereby improving overall system reliability and operational flexibility [5]. Electric vehicles (EVs) play a significant role in addressing energy shortages and reducing environmental pollution. In DC microgrid-based EV systems, however, conventional power batteries suffer from inherent limitations such as low power density, slow charging capability, and degraded performance at low temperatures, which restrict large-scale EV deployment [6]. Hybrid energy storage systems (HESS), combining power batteries with supercapacitors, offer an effective solution by enabling efficient energy recovery during regenerative braking, enhancing dynamic response, and mitigating high current stress on the battery. As a result, HESS improves battery lifespan, operational reliability, and overall performance of EV-integrated DC microgrids [7].

In energy storage system, batteries play an important role owing to their characteristics, such as high energy density and prolonged cycle life. Nevertheless, battery longevity is compromised while subjected to high-frequency components.The SC is a high-power-density device characterized by rapid charge/discharge rates and a long cycle life [8]. Batteries combined with SCs are a hybrid combination; this configuration is more popular than a single storage device, as it eliminates so many issues [9]. Conventional energy storage systems, exemplified by batteries, are constrained by challenges such as protracted charging durations and finite operational longevity. Alternative energy storage methodologies, including mechanical, electrochemical, and electromagnetic paradigms, which harness energy in diverse forms, typically incur elevated costs and necessitate intricate system architectures [10]. The un-

The associate editor coordinating the review of this manuscript and approving it for publication was Diego Rivelino Espinoza Trejo (*Corresponding author: Siddhartha Bomma).*

Siddhartha Bomma, and Udaya Bhasker Manthati are with the Department of Electrical Engineering, National Institute of Technology, Warangal, Telangana, 506004, India (e-mails: bs22eer2r03@student.nitw.ac.in, and ub@nitw.ac.in).

predictability in power output from renewable energy sources creates demands for maintaining energy network stability. The need for rapid-response energy storage solutions has led to increased adoption of SCs as an alternative storage technology, particularly in renewable energy systems and electric vehicles. [7], [11]. By using SCs, precise mitigation of power fluctuations in clean energy systems can be achieved.

An energy storage system (ESS) is essential for ensuring stable performance of photovoltaic (PV) sources when they are connected to a microgrid. The ESS helps smooth out the intermittent nature of PV power output, which in turn improves overall power quality, strengthens system stability, maintains steady dc bus voltage, and contributes to frequency regulation [3]. These benefits make it much easier to reliably incorporate solar generation into the grid. Owing to their complementary characteristics—where batteries provide high energy density and SCs offer rapid dynamic response—battery–supercapacitor HESSs have received significant interest in recent years. In these hybrid setups, batteries and SCs are given distinct responsibilities for handling power based on their individual performance traits. Nevertheless, the main difficulty lies in effectively and dynamically distributing the variable power demand between the two storage components in a coordinated manner [11]. To achieve frequency-based current diversion, the variation in filter bandwidth and its effects on the system must be addressed.

In a centralized control strategy, the photovoltaic (PV) power is measured by a central controller, which applies signal-processing techniques to decompose the fluctuating power into low-frequency and high-frequency components. Based on this decomposition, power reference commands are transmitted to the hybrid energy storage system via a communication network [4]. Centralized control methods can be broadly classified into filter-based and optimization-based approaches. In filter-based control, the power fluctuation demand is separated into low-frequency and high-frequency components, which are handled by the battery and the supercapacitor, respectively. Commonly adopted filtering techniques include high-pass and low-pass filters (HPF/LPF), wavelet transform (WT), empirical mode decomposition (EMD), and sliding average (SA) . Optimization-based control approaches allocate power within the hybrid energy storage system using advanced control techniques such as model predictive control (MPC), artificial neural networks (ANN), and fuzzy logic control (FLC). These methods optimize the power-sharing behavior by considering system dynamics, constraints, and performance objectives [12].

Recent advancements in control methodologies have been widely explored for photovoltaic (PV) systems integrated with hybrid energy storage systems (HESS). Sliding Mode Control (SMC) is frequently adopted due to its ability to provide fast dynamic response and robustness against system disturbances. However, the conventional SMC technique suffers from the chattering phenomenon, which can degrade system performance and reliability [13]. In addition, hybrid control approaches combining proportional–integral (PI) control with sliding mode control often require complex modeling and controller design procedures [14]. Fuzzy Logic Controllers (FLCs) have also been implemented in HESS-based PV systems to enable advanced power management strategies, allowing efficient power sharing among storage elements and effective regulation of the DC bus voltage. Despite these advantages, the performance of FLCs largely depends on expert knowledge for rule formulation and often requires continuous tuning as system conditions change [15]. Model Predictive Control (MPC) has gained significant attention in DC microgrid applications because of its capability to handle multi-input converter systems and optimize control performance [16]. MPC-based strategies can significantly enhance system dynamics while ensuring optimal power distribution in hybrid storage architectures [17]. Nevertheless, practical implementation of MPC generally demands high computational capability and sophisticated optimization algorithms [18]. A deadbeat control approach for PV systems operating within DC microgrids and integrated with HESS has been proposed in [19]. This technique calculates the duty cycle in a single computational step, enabling rapid control action. However, when a low-pass filter (LPF) is incorporated within the predictive control framework, it introduces a delay in generating the reference current, which may adversely affect the transient response of the DC bus voltage. Most existing works consider a fixed bandwidth. In HESS designs, it is crucial to consider the battery current rate and SC voltage levels. In dynamic conditions, conduction losses increase with high frequency supercapacitor currents [19].

To overcome the above challenges and improve the dynamic response of the energy storage system under different SC voltages under a constant bandwidth, a variable bandwidth scheduling strategy is proposed using Variable bandwidth low pass filter. This approach extends the conventional fixed bandwidth and decomposing the reference currents into the duty-cycle generation. As a result, DC bus voltage fluctuations induced by lower SC voltages compensated rapidly and accurately.

This paper presents variable bandwidth filter (VBWF) based current sharing between battery and SC. Voltage of the SC affects the SC reference current. This approach makes utilization of SC voltage fully. Battery health is preserved by mitigating current stress, as high-frequency current components are diverted to the SC. This work shows the contributions as such

1) Variable bandwidth filter based on SC voltage for HESS currents decomposition.
2) Maintaining less ripples in dc voltage regulation under all SC voltage levels.
3) With the proposed VBWF , balanced power sharing, and voltage variations are minimized under PV and load disturbances, yielding faster settling and enhanced system dynamics.
4) As the battery suffers with high-frequency components, the battery error component is transferred to SC.

The structure of this paper is organized as follows. Section II deals with system description. Section III elucidates the system configuration alongside the proposed control strategy for the HESS. Section IV describes proposed variable bandwidth scheduling strategy for the HESS. Section V presents

small signal modeling. Simulation outcomes and case studies conducted in MATLAB Simulink are presented in Section VI, while Section VII provides the corresponding hardware experimental verification. Finally, Section VIII encapsulates the primary findings and offers concluding remarks.

II. System Description and Modeling

PV source is connected to dc microgrid through boost converter. PV power is volatile in nature, therefore energy storage is important to make system stable. The structure of the system shown in Fig. 1. The DC bus architecture facilitates the integration and decoupling of energy storage systems and DC loads. To fully exploit the complementary characteristics of different storage technologies and extend their service life, hybrid energy storage systems (HESSs) combining batteries and supercapacitors are widely adopted. Fig. 1 shows a general structure of a dc microgrid.

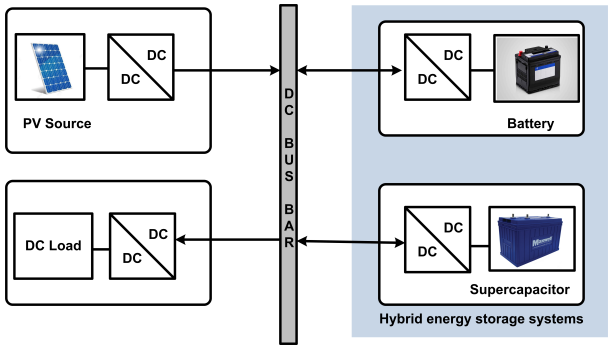

Fig. 1. Structure of the DC microgrid integrating PV generation and a battery–supercapacitor-based HESS.

A. SC modeling

Fig. 2 shows simplified electrical equivalent SC circuit, based on its voltage–current characteristics, is considered in this work [20]. Due to its structural simplicity and reasonable modeling accuracy, this representation is widely adopted in power electronic applications and real-time energy management studies. The model includes a series resistance (R_{series})

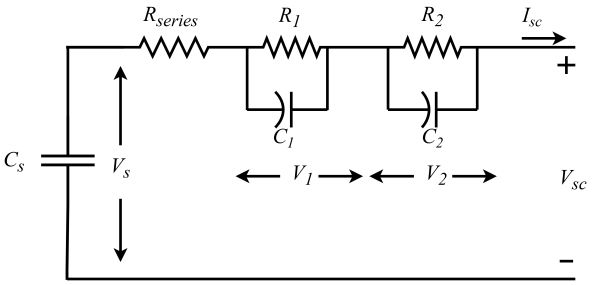

Fig. 2. Two-RC-branch electrical equivalent circuit model of supercapacitor.

along with two parallel RC branch networks, which capture the dynamic behavior of the SC, particularly its transient response. The SC voltage is given by

$$V_{sc} = V_s - I_{sc}R_{series} - V_1 - V_2 \tag{1}$$

The SOC of SC, which is a important constraint of SC, is calculated from Coulomb counting technique [21], and it is determined by

$$SOC_{sc}(t) = SOC_{sc}(t_0) - \frac{1}{3600 \times C_{sc}} \int i_{sc}\, dt \tag{2}$$

where $SOC_{sc}(t_0)$ indicates starting charge level of the SC, and C_{sc} specifies nominal storage capacity.

III. System Configuration and Control Strategy

The topology of the proposed autonomous system is depicted in Fig. 3. Fig. 1 depicts the conceptual system architecture, whereas Fig. 3 presents the simplified experimental and simulation platform used for proposed control strategy. In this configuration, a dedicated boost converter is employed to interface the PV source with the DC bus. The HESS, consisting of a battery and a SC, is connected to the DC bus through two non-isolated bidirectional buck–boost converters. The bidirectional capability of these converters allows controlled power exchange during both charging and discharging modes.

The variables V_{pv}, V_{sc}, and V_{bat} denote the PV, SC, and battery voltages, respectively, while C_{dc} represents the DC bus output filter capacitor. Switches S_1–S_4 correspond to the semiconductor devices of the battery and SC converters. The PV boost converter operates under a maximum power point tracking (MPPT) scheme based on the perturb-and-observe (P&O) algorithm [10] to ensure optimal power extraction. The respective duty cycle is applied to PV boost converter switch S_5.

A. Design of non Isolated Bidirectional Buck Boost Converter for Battery and SC

The non isolated buck boost bidirectional converter is designed by equations from [22]. The analysis is carried out under the assumption that the converter operates in continuous conduction mode, the inductors L_{bat} and L_{sc} are designed by

$$L = \frac{V_0 \cdot D}{\Delta i_{in} \cdot f_{sw}} \tag{3}$$

Where f_{sw} is switching frequency, D is duty ratio, ΔI_{in} is ripple current in inductor, and V_0 is output voltage, Capacitor is designed by

$$C = \frac{V_0 \cdot D}{\Delta V_0 \cdot f_{sw} \cdot R_L} \tag{4}$$

Where R_L is load resistance, and ΔV_0 is ripple in output voltage. Fig. 3 presents a simplified laboratory/simulation implementation of the proposed system for validating the HESS control strategy. The DC-Load interfacing converter shown in Fig. 1 is omitted because the objective of work is to evaluate the voltage regulation and power-sharing capability of the proposed control strategy under controlled load disturbances. A variable resistive load is employed to generate repeatable step changes in power demand.

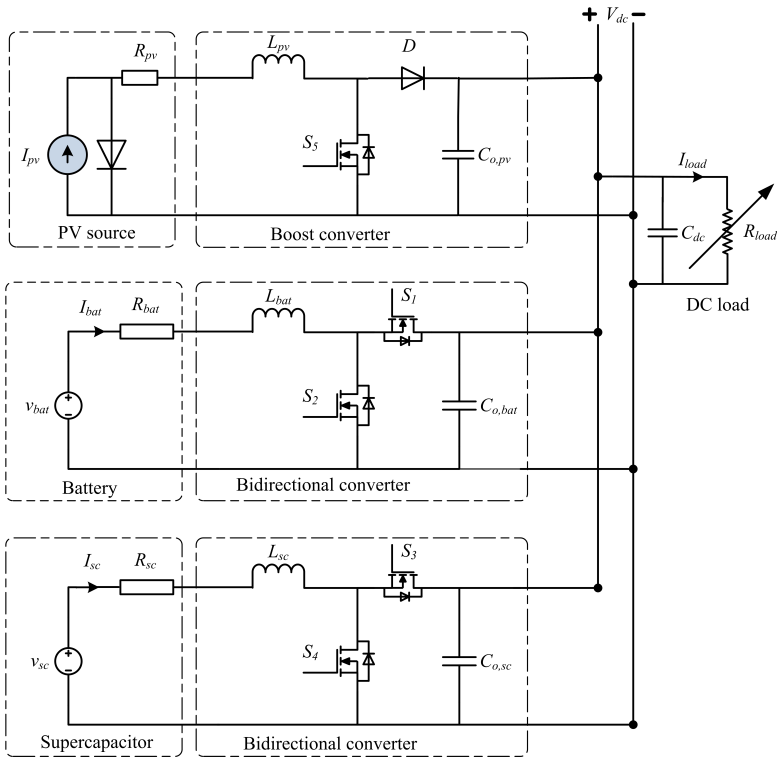

Fig. 3. Configuration of the battery–supercapacitor-based hybrid energy storage system integrated with the DC bus through bidirectional DC–DC converters.

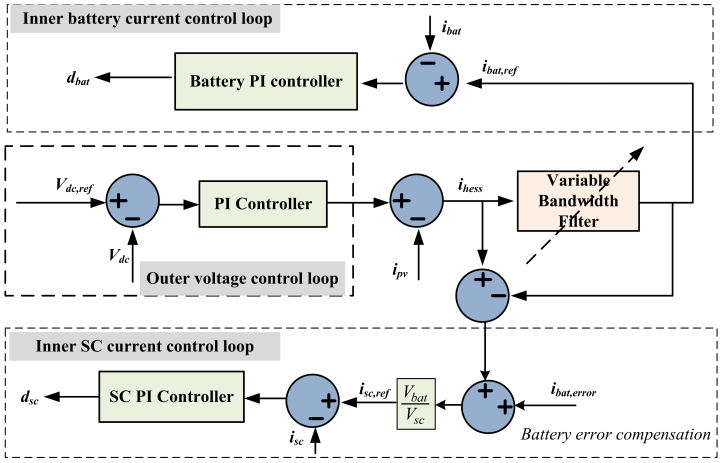

Fig. 4. Block diagram of the proposed variable-bandwidth control strategy for Hybrid energy storage system power sharing and DC bus voltage regulation.

B. Power Balance and SC Reference Current Generation Strategy

This section provides the approach for generating reference currents for battery and SC using Variable bandwidth filter. The categorization process is described by (5)–(20). In Fig. 3 at the DC-link, power balance equation is given by

$$P_{\text{pv}}(t) = P_{\text{load}}(t) + P_{\text{hess}}(t) + P_{\text{loss}}(t) \tag{5}$$

where $P_{\text{pv}}(t)$ is PV power generated, $P_{\text{hess}}(t)$ is power supplied/ delivered by hess, $P_{\text{load}}(t)$ is load power, and $P_{\text{loss}}(t)$ is power losses. $P_{\text{hess}}(t)$ is given by

$$P_{\text{hess}}(t) = P_{\text{pv}}(t) - P_{\text{load}}(t) - P_{\text{loss}}(t) \tag{6}$$

HESS power is the net power demand or supply, it is sum of battery and SC power is expressed as:

$$P_{\text{net}}(t) = P_{\text{hess}}(t) = P_{\text{bat}}(t) + P_{\text{sc}}(t) \tag{7}$$

P_{hess} contains high frequency power components and low frequency power components. It is given by

$$P_{\text{hess}}(t) = \bar{P}_{\text{hess}}(t) + \tilde{P}_{\text{hess}}(t) = V_{\text{dc}} \cdot i_{\text{hess}}(t) \tag{8}$$

Where $\bar{P}_{\text{hess}}(t)$ is average power of hess, $\tilde{P}_{\text{hess}}(t)$ transient power of HESS. HESS current is the sum of the average and

transient current components is expressed as:

$$i_{\text{hess}}(t) = \frac{\bar{P}_{\text{hess}}(t)}{V_{\text{dc}}(t)} + \frac{\tilde{P}_{\text{hess}}(t)}{V_{\text{dc}}(t)} = \bar{i}_{\text{average}}(t) + \tilde{i}_{\text{tran}}(t) \quad (9)$$

The net current by battery and SC is decoupled in two components, based on frequency components is expressed as:

$$\bar{i}_{\text{avg}}(s) = i_{\text{hess}}(s)\, G_{\text{VBWF}}(s) \quad (10)$$

Average current should be supplied or delivered by battery is given by

$$i_{\text{bat,ref}}(s) = i_{\text{hess}}(s)\, G_{\text{VBWF}}(s) \quad (11)$$

where G_{VBWF}=$(w_{variable}/(s + w_{variable}))$ is first order low pass filter with a variable cutoff frequency of for proposed system. Remaining currents should be supplied or delivered by SC as follows:

$$i_{sc} = i_{hess} - i_{\text{bat}}. \quad (12)$$

Fig. 5 shows the algorithm to split the currents based on the SC voltage. Due to battery internal dynamics, remaining uncompensated power should be compensated by SC as follows

$$P_{sc} = P_{bat,uncompensated} \quad (13)$$

$$P_{bat,uncompensated} = i_{sc} v_{bat} \quad (14)$$

where i_{sc} is actually a current derived on the battery-voltage side (i.e., from i_{sc}=i_{hess}-i_{bat}, computed using v_{bat}), then to express this as a true current on the SC side. To preserve power equivalence, i.e., the power represented by i_{sc} at the battery voltage level equals the power represented by $i_{sc,ref}$ at the actual SC voltage level is given by

$$P_{sc} = i_{sc} v_{bat} \quad (15)$$

$$i_{sc,ref} v_{sc} = i_{sc} v_{bat} \quad (16)$$

$$i_{sc,ref} = i_{sc} \frac{v_{bat}}{v_{sc}} \quad (17)$$

From Eq.(12), the Uncompensated current is given by

$$i_{sc,ref} = (i_{hess} - i_{bat})\, \frac{v_{bat}}{v_{sc}} \quad (18)$$

$$i_{sc,ref} = (i_{hess} - i_{bat,ref} + i_{bat,error})\, \frac{v_{bat}}{v_{sc}} \quad (19)$$

$$i_{sc,ref} = ((1 - G_{VBWF}(s)))\, i_{hess} + (i_{bat,error}))(v_{bat}/v_{sc}) \quad (20)$$

IV. Proposed Variable Bandwidth Filter

The purpose of variable BW filter is to generate the reference currents to battery and supercapacitor based on SC voltage. SC reference current tracks poor dynamic performance as SC takes load at lesser voltage levels. The consequence is unnecessary ripples produced by SC to the load. By implying the variable band width filter this problem can be avoided.

SC reference current tracks poor dynamic performance as SC takes load at lesser voltage levels. The consequence is unnecessary ripples produced by SC to the load. By implying the variable band width filter this problem can be avoided.

VBWF changes its cut off frequency based on the voltage of SC. As SC voltage is reducing bandwidth is increased such that at any cut of frequency reference currents is diverted to battery, and SC. Therefore SC currents tracks high frequency currents according to its voltage based on bandwidth selection. Fig. 5 gives flow chart of BW selection algorithm. Bandwidth 1 = 125 rad/sec, Bandwidth 2 = 1000 rad/sec, Bandwidth 3 = 1500 rad/sec, Bandwidth 4= 3000 rad/sec, and Bandwidth 5= 5000 rad/sec.

A. Selection of Discrete Bandwidth Levels

Instead of continuously varying bandwidth, the proposed work approximates the nonlinear function using five operating regions given in Eq.(21). In proposed control strategy

$$\omega_{\text{variable}} = \begin{cases} 125 \text{ rad/sec}, & V_{SC} > 0.75\, V_{\text{rated}}, \\ 1000 \text{ rad/sec}, & 0.50\, V_{\text{rated}} < V_{SC} \le 0.75\, V_{\text{rated}}, \\ 1500 \text{ rad/sec}, & 0.35\, V_{\text{rated}} < V_{SC} \le 0.50\, V_{\text{rated}}, \\ 3000 \text{ rad/sec}, & 0.25\, V_{\text{rated}} < V_{SC} \le 0.35\, V_{\text{rated}}, \\ 5000 \text{ rad/sec}, & V_{SC} \le 0.25\, V_{\text{rated}}. \end{cases} \quad (21)$$

This piecewise implementation simplifies the digital implementation, reduces computational burden, avoids abrupt controller instability, provides sufficient dynamic improvement. The bandwidth cut off variable values were selected considering the dynamic characteristics of the HESS converter and the sampling frequency is given by

$$\omega_{variable} = \omega_{\min} + (\omega_{\max} - \omega_{\min}) \left(\frac{V_{SC,\max} - V_{SC}}{V_{SC,\max} - V_{SC,\min}} \right)^n \quad (22)$$

where n is a sensitivity parameter. For $n > 1$ (e.g., 1.2, 1.5, 2), convex (accelerating) mapping keeps the bandwidth relatively low while V_{SC} is still high, and then increases it more rapidly as V_{SC} decreases. The lowest bandwidth of 125 rad/s ensures smooth battery current under high V_{SC} conditions. As the SC voltage decreases, progressively larger bandwidths are employed to reduce the time constant of the variable bandwidth filter and improve the transient response of the generated reference currents. The upper limit of 5000 rad/s was selected because further increases produced negligible improvement in settling time while increasing high-frequency noise sensitivity and switching ripple.

B. Effect of Variation of Supercapacitor Voltage on Variable Frequency

At any instant, SC power capability is limited by its voltage and current rating is given by

$$P_{sc}(t) = V_{sc}(t) i_{sc,ref}(t) \quad (23)$$

$$i_{sc,max}(t) = \frac{P_{sc,rated}}{V_{sc}(t)} \quad (24)$$

where $i_{sc,max}(t)$ is maximum SC current. As V_{sc} drops, $i_{sc,max}$ for a given power rises; therefore, the SC becomes less able to absorb low-frequency, high-energy currents without exceeding current limits or ripple targets. Since $[1-G_{VBWF}(s)]$ is a high-pass filter, raising ω_{variable} shrinks the frequency band handed to the SC, forcing it to carry only the highest-frequency, lowest-energy components. That is the physical reason the bandwidth must increase as V_{sc} falls.

Using Parseval's theorem, for a given load current spectrum $I_{hess}(s)$, the SC RMS current is given by

$$I_{sc,rms}^{2*} = \frac{1}{\pi}\int_0^{\infty}\left|1-\frac{\omega_{\text{variable}}}{j\omega+\omega_{\text{variable}}}\right|^2 |I_{hess}(\omega)|^2\, d\omega \quad (25)$$

$$= \frac{1}{\pi}\int_0^{\infty}\frac{\omega^2}{\omega^2+\omega_{\text{variable}}^2}|I_{hess}(\omega)|^2\, d\omega \quad (26)$$

Computing this numerically for the actual load profile, the FFT of i_{hess} is obtained for each candidate ω_{variable}. Since $i_{sc,ref,rms}(\omega_{\text{variable}})$ decreases monotonically as ω_{variable} increases, ω_{variable} is selected at each SC voltage tier such that $I_{sc,rms} \leq I_{sc,rated}$.

V. Small Signal Modeling

In order to guarantee stable operation, the dc-link voltage is tightly regulated, thereby ensuring that the instantaneous power balance between the generation and load sides is maintained. In all the considered control strategies, the controllers are designed to achieve the desired gain margin and phase margin for each of the three interfaced converters battery, SC and PV converter.

In a cascade control structure, the inner control loops are designed prior to the outer loop, as the outer-loop design relies on the inner loop exhibiting sufficiently fast and stable dynamics. Accordingly, the controller design procedure for the inner and outer loops is elaborated in systematic manner in subsections Proposed system has three PI controllers as shown in Fig. 6

1) SC inner current loop
2) Battery inner current loop
3) Outer DC-bus voltage loop

In the proposed VBWF control, the inner current loops are designed first, followed by the outer dc-link voltage loop, since the outer-loop design assumes that the inner loops exhibit sufficiently fast and stable dynamics. The VBWF is incorporated between the outer voltage loop and the battery and SC inner current-control loops to generate the reference currents for the battery and SC. Since the PV, battery, and SC converters operate in boost mode, their corresponding duty to output current transfer functions exhibit a right half plane (RHP) zero. Therefore, the converter control-loop bandwidth is selected sufficiently below the RHP-zero frequency to maintain adequate stability margins.

The current control loop bandwidth of the SC converter is restricted to one-sixth of the switching frequency to avoid subharmonic oscillations, which can be expressed as

$$\omega_{ci,SC} \leq \frac{\omega_{sw}}{6}. \quad (27)$$

In the small-signal analysis, the PV-side disturbance is assumed to be zero. This is for simplifying the complexity, and nature disturbance is similar with battery and SC converter in influencing the dc-link voltage dynamics. Consequently, the dominant contribution of the SC converter to the dc-link voltage response is considered in the small-signal model. The controller parameters are designed based on the SC power stage, owing to its higher charge and discharge rates compared with those of the battery. To ensure stable operation of the system, the converter control-loop bandwidth is selected sufficiently lower than the frequency of the converter control-loop bandwidth is selected such that

$$\omega_{bw} \ll \omega_{z,\text{RHP}}. \quad (28)$$

This constraint prevents the control bandwidth from approaching the RHP-zero frequency, thereby maintaining adequate stability margins and avoiding undesirable dynamic interactions.

A. Design of SC PI Controller

Given the rapid power variations characteristic of the SC, its current control loop is deliberately designed with the fastest response time among the control loops employed in the system. As shown in Fig. 3, a bidirectional dc–dc converter connects the SC to the dc link. In the context of controller design, this converter is assumed to function in the boost mode.

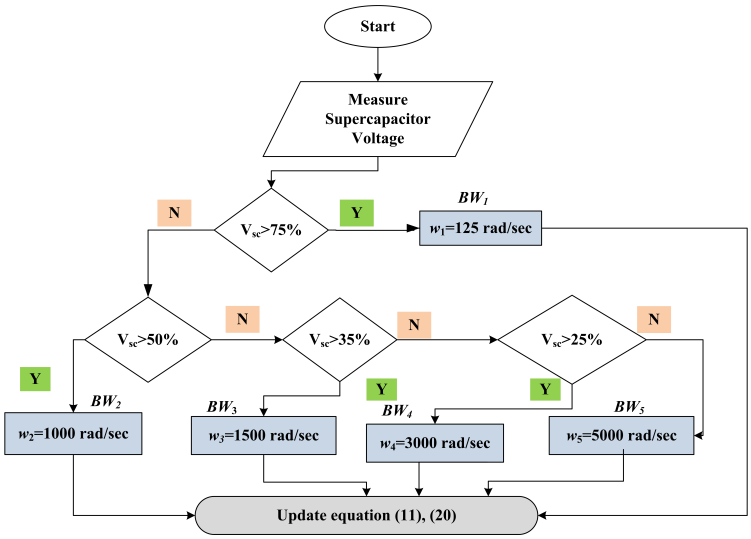

Fig. 5. Flowchart illustrating the operation of the proposed variable-bandwidth filter.

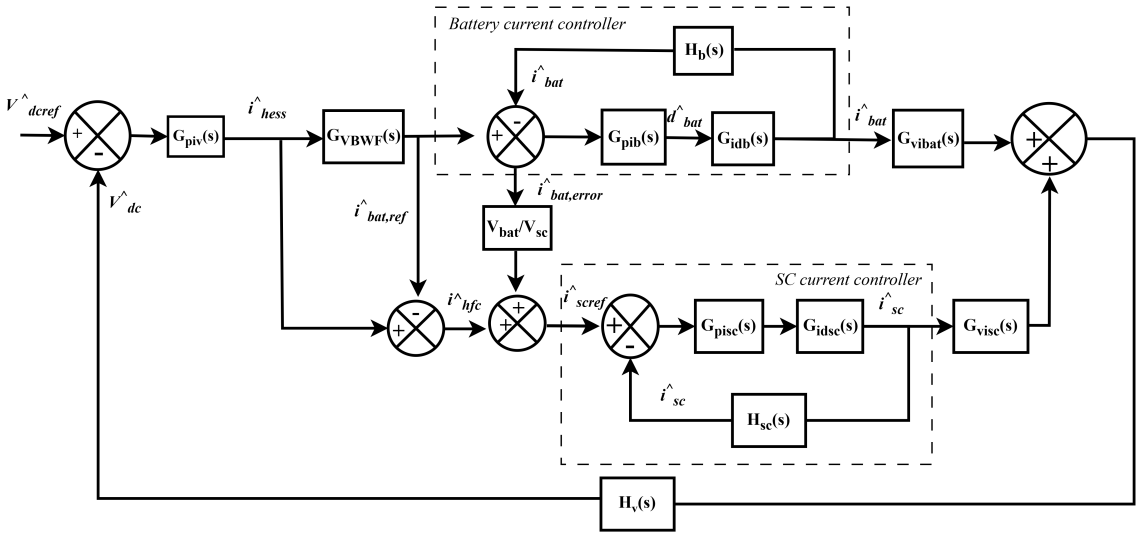

Fig. 6. Simplified control-loop representation for frequency-domain analysis.

In this configuration, the converter SC current is sensed and fed back to the current error amplifier through the feedback gain H_{sc}, which is equal to 1. The SC current error is then processed by a proportional–integral (PI) controller. The controller output is subsequently applied to the pulse-width modulation (PWM) block, which generates the corresponding gate pulses for switches S_3 and S_4. Considering i_{sc} as the SC current and d_{sc}as the converter duty ratio, SC duty to current transfer function be expressed as follows [23]:

$$G_{i_{d_sc}}(s) = \frac{\tilde{i}_{sc}}{\tilde{d}_{sc}} = \frac{V_{dc}C_{dc}s + 2\frac{V_{dc}}{R_l}}{L_{sc}C_{sc}s^2 + \frac{L_{sc}}{R_l}s + (1 - D_{sc})^2} \tag{29}$$

Uncompensated SC current-control loop is given by

$$G_{sc,\text{uncomp}}(s) = G_{ids}(s)H_{sc}(s) \tag{30}$$

Where $H_{sc}(s)$ denotes the SC current-feedback gain, $H_{sc}(s) = 1$. The system exhibits stable open-loop charac-

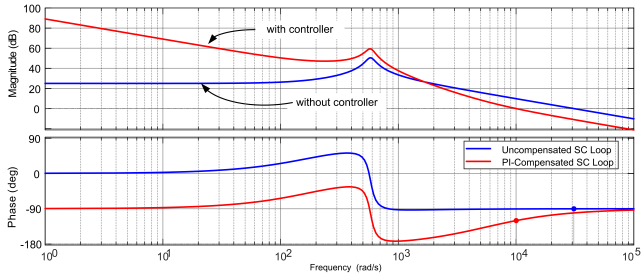

Fig. 7. Bode plot of SC current control loop with and without compensation.

teristics, with a phase margin of approximately $90°$ at a gain crossover frequency of 30.1 krad/s, while the gain margin is infinite. For adequate frequency separation between the current-control loop dynamics and the converter switching frequency, the SC current controller bandwidth is designed to be approximately one-sixth of the switching frequency, w_{sw}, thereby reducing the possibility of subharmonic oscillations and must be less than $\omega_{z,\text{RHP}} = 10.7736 \times 10^3$ rad/s Therefore, the required bandwidth for this controller is chosen as 10 krad/s along a safe phase margin of $60°$. Based on these design, the proportional and integral gains for SC uncompensated loop are obtained as $K_p = 0.28$ and $K_i = 1600$, respectively, using the MATLAB PID Tuner. The transfer function of PI controller employed is given by

$$G_{pi,sc}(s) = K_{p,sc} + \frac{K_{i,sc}}{s} \tag{31}$$

SC compensated loop get high Bandwidth and stable operation under these conditions. Compensated SC current control loop is given by

$$G_{sc,comp}(s) = G_{pi,sc}(s)G_{i_{d_sc}} \tag{32}$$

B. Design of Battery PI controller

Battery converter current control loop must be faster than voltage control loop and less than SC current loop. Similar to SC control the battery current controller is designed. The PWM signal drive switches s_1 and s_2. Battery converter duty to current transfer function expressed as follows [24]:

$$G_{idb} = \frac{\tilde{i}_{bat}}{\tilde{d}_{bat}} = \frac{v_{dc}C_{dc}s + 2\frac{v_{dc}}{R_l}}{L_{bat}C_{dc}s^2 + \frac{L_{bat}}{R_l}s + (1 - D_{bat})^2} \tag{33}$$

uncompensated battery current-control loop is given by

$$G_{bat,\text{uncomp}}(s) = G_{idb}(s)H_b(s) \tag{34}$$

where $H_b(s)$ is the battery current-feedback gain, and $H_b(s) = 1$. Fig. 8 shows the Bode plot of the uncompensated and compensated battery current-control loop. The uncompensated loop exhibits a phase margin (PM) of $90°$ and an infinite gain margin (GM), with a gain crossover frequency of approximately 30×10^3 rad/s. To achieve a suitable trade-off between dynamic response and stability, the desired gain crossover frequency is selected as approximately 6×10^3 rad/s with a target PM of $60°$. Based on these design specifications, the PI-controller gains are obtained using the MATLAB PID Tuner as $K_p = 0.16$ and $K_i = 570$.

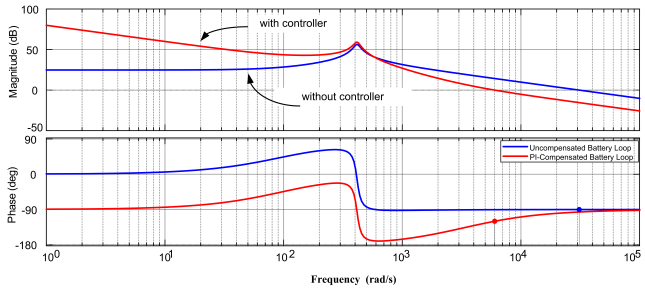

Fig. 8. Bode plot of battery current control loop with and without compensation.r

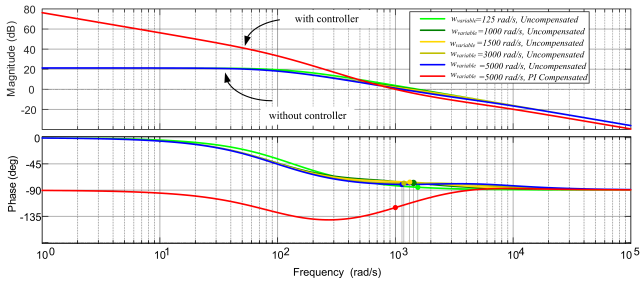

Fig. 9. Bode plot of voltage control loop with and without compensation.

The PI controller employed for the battery current-control loop is given by

$$G_{pib}(s) = K_{pb} + \frac{K_{ib}}{s} \tag{35}$$

The open-loop transfer function of the compensated battery current-control loop is given by

$$G_{bat,compensated}(s) = G_{pib}(s)G_{idb}(s) \tag{36}$$

C. Design of Outer Voltage PI Controller

Owing to the significantly higher speed of the inner current loops relative to the outer voltage loop, within the outer loop's bandwidth of interest, $G_{idb_{cl}}(s) \approx 1$, $G_{ids_{cl}}(s) \approx 1$, therefore $i_{bat,error} \approx 0$. This makes the feed-forward correction term negligible for the outer-loop derivation. The voltage control loop is designed such the battery converter and SC converter's current to voltage transfer function kept in the loop design. $H_v(s)$ denotes the output voltage feedback gain, $H_v(s) = 1$ Uncompensated open loop voltage gain of dc voltage control from small signal model is expressed as follows:

$$G_{vdc_uncomp}(s) = G_{VBWF}(s)G_{idb_cl}(s)G_{vib}(s) + [1 - G_{VBWF}(s)]\, G_{idsc_cl}(s)G_{vis}(s). \tag{37}$$

$$G_{VBWF}(s) = \frac{w_{variable}}{S + w_{variable}} \tag{38}$$

$$G_{idb_{cl}}(s) = \frac{G_{pib}(s)G_{idb}(s)}{1 + G_{pib}(s)G_{idb}(s)H_b} \tag{39}$$

$$G_{ids_{cl}}(s) = \frac{G_{pis}(s)G_{ids}(s)}{1 + G_{pis}(s)G_{ids}(s)H_s} \tag{40}$$

$$G_{vis} = \frac{R_l(1 - D_{sc})(1 - \frac{L}{R(1-D_{sc})^2})}{2 + R_l C_{dc} S} \tag{41}$$

$$G_{vib} = \frac{R_l(1 - D_{bat})(1 - \frac{L}{R(1-D_{bat})^2})}{2 + R_l C_{dc} S} \tag{42}$$

where $G_{VBWF}(s), G_{idb_{cl}}(s), G_{ids_{cl}}(s), G_{vis}(s), G_{vib}(s)$ are transfer functions of VBWF, battery closed loop, SC closed loop, SC current to voltage, battery current to voltage respectively. The uncompensated and compensated frequency-response characteristics of the outer voltage control loop are shown in Fig. 9. The bode plot is constructed at different bandwidths according to Eq. (21) Furthermore, the frequency-response analysis performed for a variable bandwidth of $5000\ \mathrm{rad/s}$ results in a minimum gain crossover frequency of $1137\ \mathrm{rad/s}$. Since the phase margin decreases as the selected variable bandwidth increases, the crossover frequency of the voltage control loop is conservatively selected as $1000\ \mathrm{rad/s}$. This value is also sufficiently lower than the minimum RHPZ frequency of the converter. To provide adequate low-frequency gain while maintaining a phase margin of approximately $60°$, the voltage-loop PI compensator $G_{piv}(s)$ is designed by

TABLE I
OUTER VOLTAGE CONTROL WITH VARIABLE-BANDWIDTH DC-LINK STABILITY MARGINS

BW (rad/s)	GM (dB)	PM (deg)	ω_{gc} (rad/s)	Stability	Loop
125	∞	94.874	1552.449	Stable	Uncompensated
1000	∞	102.268	1423.856	Stable	Uncompensated
1500	∞	103.691	1324.226	Stable	Uncompensated
3000	∞	101.994	1180.903	Stable	Uncompensated
5000	∞	99.672	1137.689	Stable	Uncompensated
5000	∞	60.000	1000.000	Stable	Compensated

$$G_{piv}(s) = K_{pv} + \frac{K_{iv}}{s} \tag{43}$$

The resulting PI parameters are selected is given by

$$K_{pv} = 0.4, \qquad K_{iv} = 202 \tag{44}$$

Consequently, the compensated open-loop transfer function of the DC-link voltage control loop is expressed as follows:

$$G_{vdc,comp}(s) = G_{piv}(s)\Big[G_{VBWF}(s)G_{idb,cl}(s)G_{vib}(s) + (1 - G_{VBWF}(s))\, G_{idsc,cl}(s)G_{vis}(s)\Big]. \tag{45}$$

DC bus voltage is controlled by minimizing the error difference of actual voltage and desired output voltage. Here the error is reduced by linear controller i. e PI control , the tuning parameters are calculated by using MATLAB PID tuner tool. All configurations are stable, with infinite GM and PM ranging from approximately $94.9°$ to $103.7°$.Compensated Voltage control loop is stable with a PM of $60°$ with infinite gain.

VI. SIMULATION RESULTS

This section presents simulation results of a Variable bandwidth low pass filter approach for power sharing and voltage regulation in HESS for solar PV-Fed DC microgrids. The simulation is carried out in MATLAB Simulink platform.

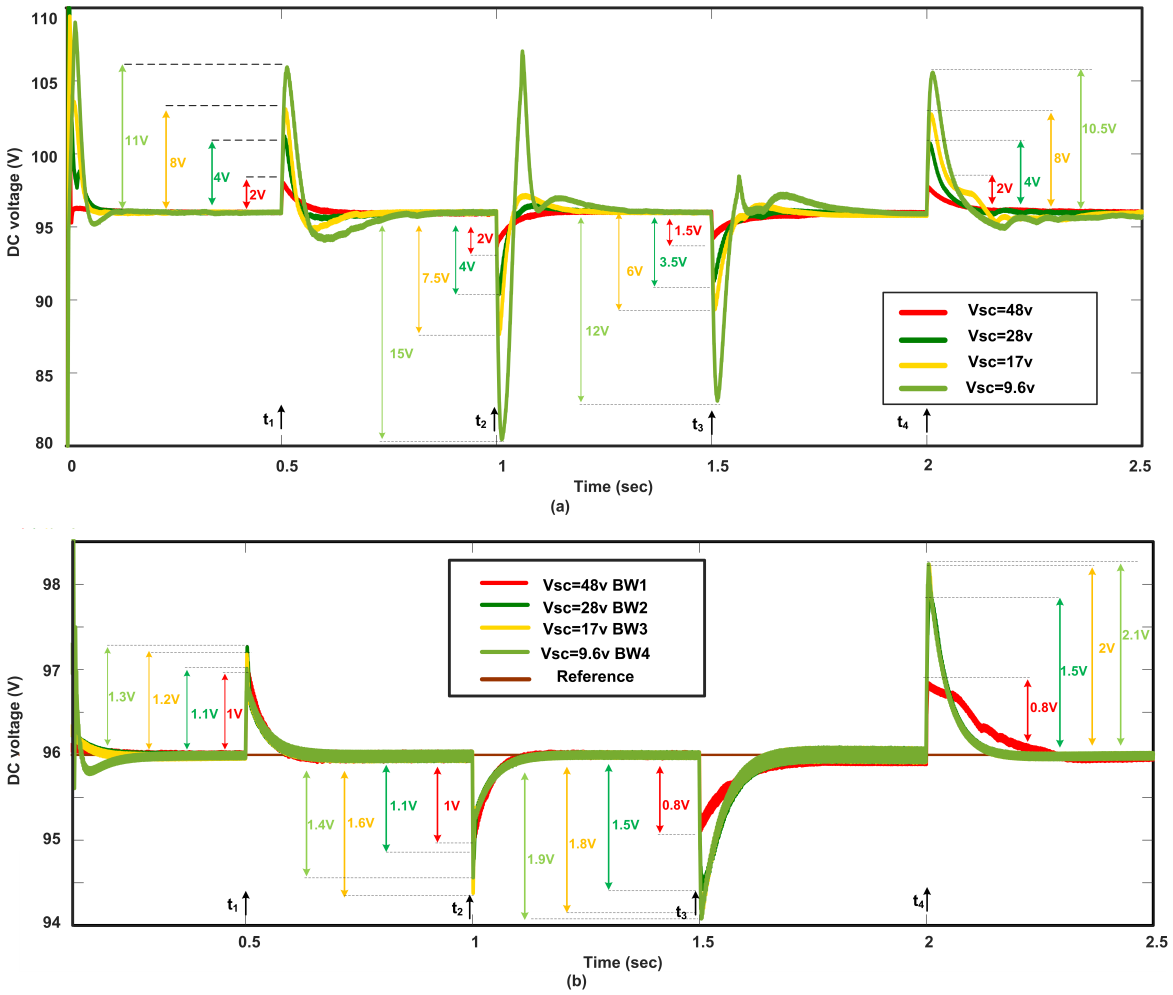

Fig. 10. (a).DC voltage regulation at different SC voltages with CBWF (b).DC voltage regulation at different SC voltages with VBWF.

TABLE II
TUNING PARAMETERS FOR VOLTAGE AND CURRENT LOOPS

Controller	K_p	K_i
Outer voltage controller	0.4	202
Inner battery current controller	0.16	570
Inner supercapacitor current controller	0.28	1600

TABLE III
DC MICROGRID SYSTEM PARAMETERS

Parameter	**Values**
Battery unit	$V_{bat} = 48$ V, 28 Ah
SC unit	$V_{sc} = 48$ V, $C = 19.3$ F
PV panel	$V_{pv} = 60$ V, $I_{pv} = 15.8$ A
Bi-directional converters	$L_{sc} = 1.5$ mH, $L_{bat} = 1.5$ mH
	$C_{bat} = 440\,\mu$F, $C_{sc} = 440\,\mu$F
Load voltage	96 V
Switching frequency (f_{sw})	10 kHz
Rated output power	1 kW

Table III lists the detailed parameters for setup for simulations. In simulations, two cases are considered: one is CBWF, and another is VBWF. Mosfet switches are used in DC-DC converters. The lead acid battery model is taken for simulation with a rating of 48 Volts and 28 Ah rating. supercapacitor is taken with a rating of 48 volts and 58 F for better efficiency, beyond this rating SC performance may under utilized or over-performed. DC bus voltage ripple and current ripple are set to 2% and 5% respectively. The proposed system design is tested under different SC voltages by applied variable bandwidth filter at step load and source conditions for validating proposed control strategy.

In this system, firstly, a step change of generation power is applied from 100 W to 200 W at 0.5 sec with a PV current change of 4 A to 8 A and reducing it from 100 W to 200 W with a PV current change of 8 A to 4 A. Secondly, a step change of load is applied from 100 w to 200 w at 1.5 sec with a load current change of 2 A to 4 A and reducing it from 200 W to 100 W with a load current change of 4 A to 2 A at 2 sec. Fig. 11 can shows the variation in currents of system.

1) SC Reference Currents Generation with CBWF: Fig. 12 shows the reference supercapacitor current by applying generation change at 0.5 sec. It can be observe that SC reference current is taking different settling and peak overshoots at constant BW of 125 rad/sec. From SC voltage 100% to 25% , i.e 48 volts, 28 V, 17 V and 9.6 v. The reference currents getting worsen at reduced SC voltages.

2) Supercapacitor Reference Currents Generation with VBWF: Fig. 13 shows the reference supercapacitor current by

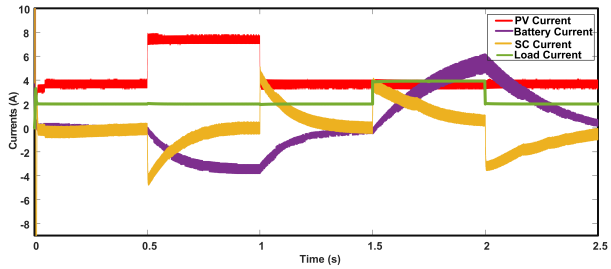

Fig. 11. HESS currents variation for step change in PV and load currents.

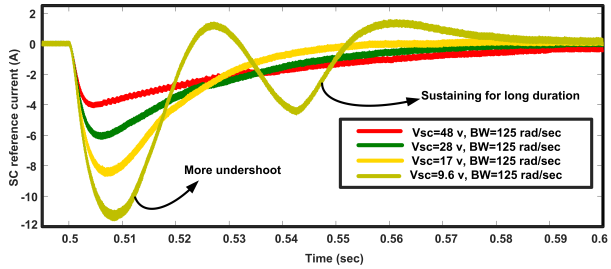

Fig. 12. Generation of SC reference currents with fixed bandwidth.

TABLE IV
PERFORMANCE COMPARISON FOR STEP CHANGE IN GENERATION

V_{sc} (V)	Constant BW		Variable BW	
	% M_p	T_s (ms)	% M_p	T_s (ms)
48	2.8	20–30	1.04	20–25
27	4.16	22–35	1.25	22–25
17	8.3	25–37	1.6	20–23
9.6	15.6	30–40	1.35	22–24

applying generation change at 0.5 sec. It can be observe that supercapacitor reference current is taking similar settling and peak overshoots at different bandwidths according to proposed VBWF from Fig. 5. From SC voltage 100% to 25% , i.e 48 volts, 28 V, 17 V and 9.6 V. The reference currents getting better at reduced SC voltages compared to the CBWF.

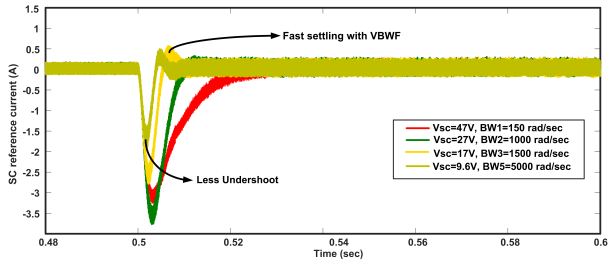

Fig. 13. Generation of SC reference currents with variable bandwidth.

3) DC Link Voltage Regulation at Different Supercapacitor Voltages with Constant Bandwidth: Fig. 10 a. shows that DC voltage regulations by applying load and generation step changes without applying VBWF. The peak overshoots and settling times are showing very poor regulation at different voltage levels with same constant bandwidth approach. The detailed comparison given in Table IV and Table V

4) DC Link Voltage Regulation at Different SC Voltages with Variable Bandwidth: Fig. 10 b. shows that DC voltage regulations by applying load and generation step changes with VBWF. After applying VBWF at different percentages of SC voltages showing better dynamic performance. The detailed comparison given in Table IV and Table V

TABLE V
PERFORMANCE COMPARISON FOR STEP CHANGE IN LOAD

V_{sc} (V)	Constant BW		Variable BW	
	% M_p	T_s (ms)	% M_p	T_s (ms)
48	2.08	25	1.0	22–26
27	3.64	27	1.5	22–26
17	6.25	25–31	2.08	21–25
9.6	12.5	30–35	2.1	22–26

5) Overall Comparison of Proposed System with Existing Works: From simulation results, the overall dynamic performance of the system at rated SC voltage with proposed control with existing control techniques are given in Table VI. This work is showing better control dynamics with considering all SC voltage ranges.

VII. EXPERIMENTAL RESULTS

In order to test proposed variable bandwidth based PI control, a prototype hardware setup was developed.The dSPACE DS1104 real-time platform is used to develop proposed system. A regulated power supply is employed to emulate the PV source [23], while a boost converter is utilized for PV current control. The battery and supercapacitor are rated at 12 V, 7 Ah (lead-acid) and 16 V, 58 F (Maxwell BMOD0058), respectively. The performance of the HESS-based microgrid is investigated under various operating conditions. The nominal DC bus voltage is set to 18 V, and the converter is designed for a power rating of 150 W. One Volatge sensor LEM LV-25, three current sensors LEM LA-25p are used for sensing voltage and currents of DC, battery, SC, and PV respectively. Fig. 18 shows the prototype experimental hardware setup. The parameter details of experimental setup is summarized in Table VII. During the experimental operation, in Generation changes, PV current is varied between 0.25 A to 1 A. The generation power varies from 4.5 W to 18 W.

A. Experimental Results under Generation change

Fig. 14 at t_1 instant and t_2 instant PV current increases from 0.5 A to 1 A, and reduced from 1 A to 0.5 A. DC bus voltage is operating at 18 volts, , battery current is decreased from 0.5 A to 0.1 A, and SC current will provide transient current for a transient duration. As voltage of supercapacitor is at 16 volts, there is no much effect of ripples on DC bus.

Fig. 15 at t_3 instant and t_4 instant PV current increases from 0.5 A to 1 A, and reduced from 1 A to 0.5 A. DC bus voltage is operating at 18 volts, battery current is decreased from 1.1 A to 0.25 A, and SC current will provide transient current for a transient duration. As voltage of SC is at 6 volts, SC voltage is less, there are ripple effect on dc bus voltage. When a step change occurs in PV power, the SC responds more rapidly than the battery, demonstrating its higher power density. Consequently, power exchange takes place between the SC and the battery.

TABLE VI
PERFORMANCE COMPARISON WITH EXISTING METHODS

Performance Metric	[25]	[23]	[26]	Proposed Control Strategy
Maximum peak overshoot	6–8%	3.8–5.5%	3.6–4.2%	1.5–2.5%
Settling time	80–120 ms	30–60 ms	20–30 ms	20–28 ms
Power splitting strategy	CBLPF	CBLPF	CBLPF	Variable-BW filter
Consideration of SC voltage variation	No	No	Partly	Yes

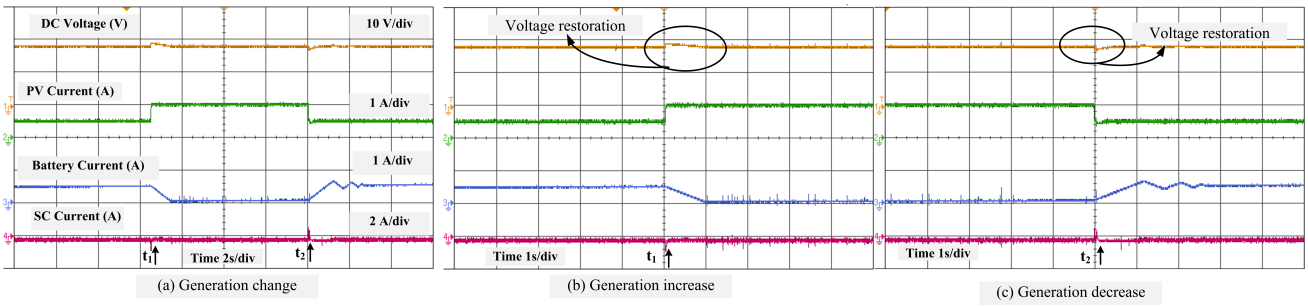

(a) Generation change (b) Generation increase (c) Generation decrease

Fig. 14. Hardware results: System performance under a PV step change at a DC voltage of 18 V for an SC voltage at 100% of its rated voltage: (a) step change, (b) enlarged view of the step increase, and (c) enlarged view of the step decrease.

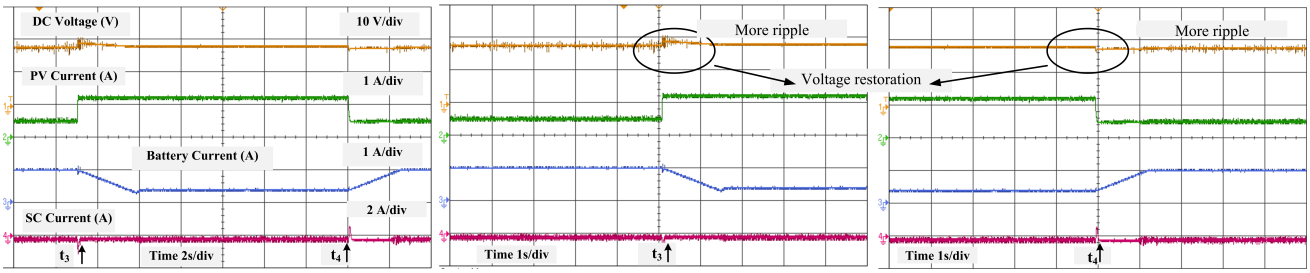

(a) Generation change (b) Generation increase (c) Generation decrease

Fig. 15. Hardware results: System performance under a PV step change at a DC voltage of 18 V for an SC voltage below 25% of its rated voltage: (a) step change, (b) enlarged view of the step increase, and (c) enlarged view of the step decrease.

TABLE VII
SPECIFICATIONS OF REDUCED-SCALE EXPERIMENTAL SETUP

Parameter	Values
Battery unit	$V_{bat} = 12$ V, 7 Ah
SC unit	$V_{sc} = 16$ V, $C = 58$ F
Emulated PV source	$V_{pv} = 12$ V, $I_{pv} = 5$ A
Bi-directional converters	$L_{sc} = 3.1$ mH, $L_{bat} = 3.1$ mH $C_{bat} = 440\,\mu$F, $C_{sc} = 440\,\mu$F
PV boost converter	$L_{pv} = 3.8$ mH, $C_{dc} = 440\,\mu$F
Load voltage	24 V
Switching frequency (f_{sw})	10 kHz
Rated output power	150 W

B. Experimental Results for DC Voltage under Different Test Conditions with CBWF

Fig. 16 shows DC bus voltage at different SC voltage levels.The DC reference voltage is taken as 18 volts. In this experimental studies, SC voltage is rated for 16 volts. Four operating voltages taken to test with conventional bandwidth filter, at 15 V, 12 V, 9 V, and 5 V respectively. A step change is generation is applied and removed for previously stated SC voltages. Observation is that, as SC voltage is dropping, it showing more ripple effect, it is taking more to settle the reference value.

C. Experimental Results for DC Voltage under Different Test Conditions with VBWF

Fig. 17 shows DC bus voltage at different SC voltage levels. The reference voltage is taken as 18 volts, for comparing both VBWF and CBWF. From experimental studies, SC is voltage is rated for 16 volts. Four SC operating voltages taken to test with variable bandwidth filter. A step change is generation is applied and removed for previously stated SC voltages. It is evident that, As even SC is voltage is dropping it showing less ripple effect and better to settling with the reference value. It is achieved by applying algorithm shown in Fig. 5.

VIII. CONCLUSION

In this paper, a novel variable bandwidth filter is proposed for hybrid energy storage system. It shows the for generation SC reference current one, to mitigate the ripple effect on dc bus voltage ensuring more robust DC bus voltage regulation during disturbances, such as the unplanned disconnection of the DC microgrid. Secondly, a voltage compensation error is added to divert transients currents to battery so battery life gets improved. Thirdly, efficient utilization of SC, as even voltage of SC drops further, we can use SC to support battery for longer period. A study cases different types of bandwidths is carried out in simulation and hardware to verify the benefits

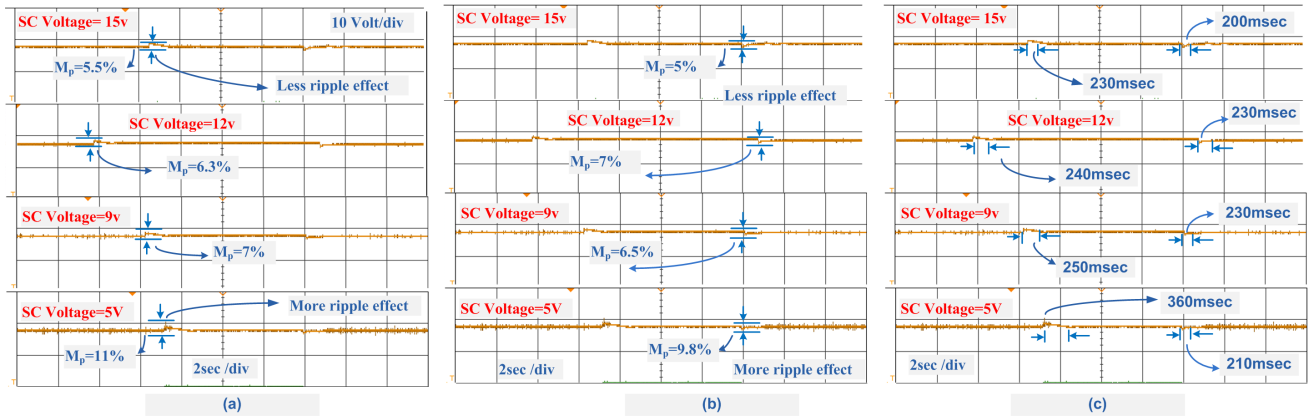

Fig. 16. Hardware results for DC voltage regulation at 18 V for different SC voltage levels using CBWF: (a) peak overshoot for a step increase in PV power, (b) peak overshoot for a step decrease in PV power, and (c) settling time.

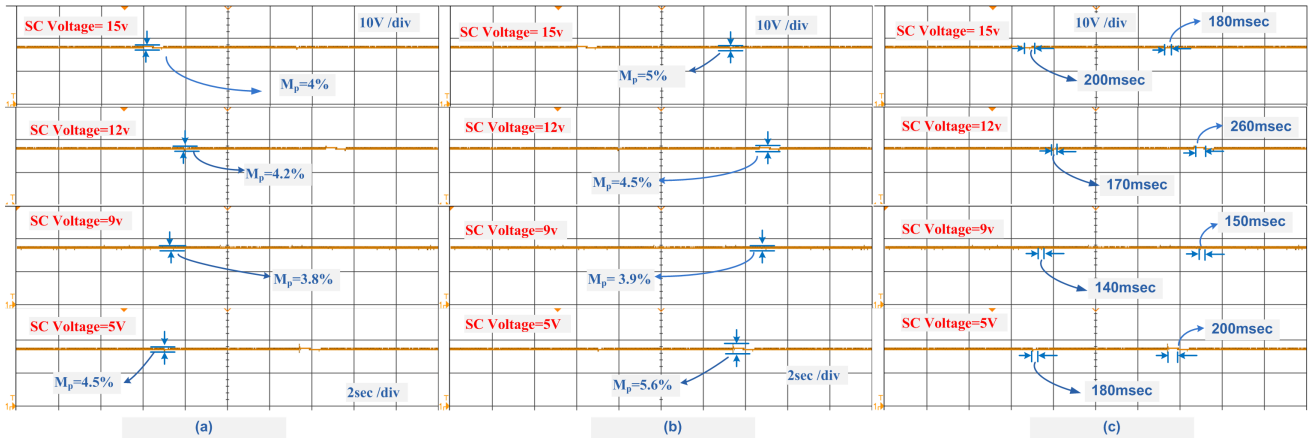

Fig. 17. Hardware results for DC voltage regulation at 18 V for different SC voltage levels using VBWF: (a) peak overshoot for a step increase in PV power, (b) peak overshoot for a step decrease in PV power, and (c) settling time

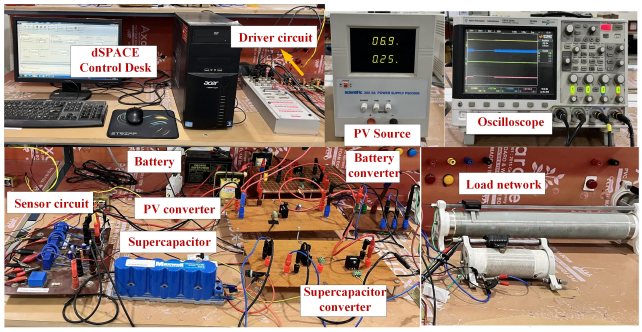

Fig. 18. Experimental setup for the proposed variable-bandwidth control strategy.

of this scheme. These results not only regulate dc bus voltage and also reduced ripple effect on it at low SC's voltages. By incorporating a variable-bandwidth filtering strategy into the HESS framework, charge–discharge stress on the SC and battery is reduced.

REFERENCES

[1] Z. Wang, L. Zhou, L. Xiong, Q. Zhou, W. Huang, H. Yang, F. Gao, and Y. Chen, "Voltage-source control for green-hydrogen hybrid energy storage system with operational constraints and current rate limiter," *IEEE Transactions on Smart Grid*, 2025, doi.org/10.1109/TSG.2025.3556988.

[2] X. Zhang, Y. Wang, X. Yuan, Y. Shen, Z. Lu, and Z. Wang, "Adaptive dynamic surface control with disturbance observers for battery/supercapacitor-basedhybridenergysources in electric vehicles," *IEEE Transactions onTransportation Electrification*, vol. 9, pp. 5165–5 181 244, 12 2023, doi.org/10.1109/tte.2022.3194034.

[3] J. D. Rios-Peñaloza, A. Prevedi, M. Prodanović, and J. Roldán-Pérez, "Central controller for photovoltaic power plants with hybrid energy storage systems providing automatic frequency restoration reserve," *IEEE Transactions on Sustainable Energy*, 2026, doi.org/10.1109/TSTE.2026.3653342.

[4] M. Mao, Y. Tang, F. Ma, H. Sun, G. Hua, and P. Li, "A three-level hierarchical power smoothing control strategy for pavement photovoltaics under vehicle shadow disturbance," *IEEE Transactions on Power Electronics*, 2025, doi.org/10.1109/TPEL.2025.3603016.

[5] S. Vazquez, S. M. Lukic, E. Galvan, L. G. Franquelo, and J. M. Carrasco, "Energy storage systems for transport and grid applications," *IEEE Transactions on industrial electronics*, vol. 57, no. 12, pp. 3881–3895, 2010, doi.org/10.1109/tte.2022.3194034.

[6] P. Ranjbaran, J. Ebrahimi, A. Bakhshai, and P. K. Jain, "A comprehensive review of topologies and energy management methods for hybrid energy storage systems in electric vehicle applications," *IEEE Transactions on Power Electronics*, 2025, doi.org/10.1109/TPEL.2025.3625535.

[7] D. A. Elalfy, E. Gouda, M. F. Kotb, V. Bureš, and B. E. Sedhom, "Comprehensive review of energy storage systems technologies, objectives, challenges, and future trends," *Energy Strategy Reviews*, vol. 54, p. 101482, 2024, doi.org/10.1016/j.esr.2024.101482.

[8] C. Arunkumar, U. B. Manthati, and S. Punna, "Supercapacitor-based transient power supply for dc microgrid applications," *Electrical Engineering*, vol. 104, no. 2, pp. 463–472, 2022, doi.org/10.1007/s00202-021-01312-7.

[9] M. B. Abdelghany, A. Al-Durra, and F. Gao, "A coordinated op-

timal operation of a grid-connected wind-solar microgrid incorporating hybrid energy storage management systems," *IEEE Transactions on Sustainable Energy*, vol. 15, no. 1, pp. 39–51, 2023, doi.org/10.1109/TSTE.2023.3263540.

[10] T. Sutikno, W. Arsadiando, A. Wangsupphaphol, A. Yudhana, and M. Facta, "A review of recent advances on hybrid energy storage system for solar photovoltaics power generation," *IEEE Access*, vol. 10, pp. 42 346–42 364, 2022, doi.org/10.1109/ACCESS.2022.3165798.

[11] Y.-L. Lee, C.-H. Lin, C.-H. Chang, H.-D. Liu, and C.-C. Chen, "A novel hybrid energy storage system with an adaptive digital filter-based energy management strategy for electric vehicles," *IEEE Transactions on Transportation Electrification*, vol. 10, no. 3, pp. 5131–5142, 2023, doi.org/10.1109/TTE.2023.3320817.

[12] X. Zhang, P. Li, Y. Zhang, D. Huang, B. Wang, Y. Zhou, F. Huo, and A. Ukil, "Reinforcement learning based active model variation deadbeat control for energy storage system in dc microgrids with constant power loads," *IEEE Transactions on Industrial Electronics*, 2025, doi.org/10.1109/TIE.2025.3610756.

[13] E. M. Asensio, G. A. Magallán, C. H. De Angelo, and F. M. Serra, "Energy management on battery/ultracapacitor hybrid energy storage system based on adjustable bandwidth filter and sliding-mode control," *Journal of Energy Storage*, vol. 30, p. 101569, 2020, doi.org/10.1016/j.est.2020.101569.

[14] P. Singh and J. Lather, "Dynamic current sharing, voltage and soc regulation for hess based dc microgrid using cpismc technique," *Journal of Energy Storage*, vol. 30, p. 101509, 2020, doi.org/10.1016/j.est.2020.101509.

[15] R. Bhosale and V. Agarwal, "Fuzzy logic control of the ultracapacitor interface for enhanced transient response and voltage stability of a dc microgrid," *IEEE Transactions on Industry Applications*, vol. 55, no. 1, pp. 712–720, 2018, doi.org/10.1109/TIA.2018.2870349.

[16] X. Zhang, B. Wang, D. Gamage, and A. Ukil, "Model predictive and iterative learning control based hybrid control method for hybrid energy storage system," *IEEE Transactions on Sustainable Energy*, vol. 12, no. 4, pp. 2146–2158, 2021, doi.org/10.1109/TSTE.2021.3083902.

[17] N.-D. Nguyen, C. Yoon, and Y. I. Lee, "A standalone energy management system of battery/supercapacitor hybrid energy storage system for electric vehicles using model predictive control," *IEEE Transactions on Industrial Electronics*, vol. 70, no. 5, pp. 5104–5114, 2022, doi.org/10.1109/TIE.2022.3186369.

[18] X. Liu, Y. Suo, Z. Zhang, X. Song, and J. Zhou, "A new model predictive current control strategy for hybrid energy storage system considering the soc of the supercapacitor," *IEEE Journal of Emerging and Selected Topics in Power Electronics*, vol. 11, no. 1, pp. 325–338, 2022, doi.org/10.1109/JESTPE.2022.3159665.

[19] X. Zhang, B. Wang, Y. Zhou, Y. Zhang, and A. Ukil, "An event-triggered deadbeat control considering dynamic power loss compensation for hybrid energy storage system," *IEEE Transactions on Industrial Electronics*, vol. 70, no. 7, pp. 6844–6855, 2022, doi.org/10.1109/TIE.2022.3201281.

[20] L. Zhang, X. Hu, Z. Wang, F. Sun, and D. G. Dorrell, "A review of supercapacitor modeling, estimation, and applications: A control/management perspective," *Renewable and Sustainable Energy Reviews*, vol. 81, pp. 1868–1878, 2018, doi.org/10.1016/j.rser.2017.05.283.

[21] H. Mahmood, D. Michaelson, and J. Jiang, "A power management strategy for pv/battery hybrid systems in islanded microgrids," *IEEE Journal of Emerging and Selected topics in Power electronics*, vol. 2, no. 4, pp. 870–882, 2014, doi.org/10.1109/JESTPE.2014.2334051.

[22] K. Tesaki and M. Hagiwara, "Control and experimental verification of a bidirectional nonisolated dc–dc converter based on switched-capacitor converters," *IEEE Transactions on Power Electronics*, vol. 36, no. 6, pp. 6501–6512, 2021, doi.org/10.1109/TPEL.2020.3040070.

[23] S. K. Kollimalla, M. K. Mishra, A. Ukil, and H. Gooi, "Dc grid voltage regulation using new hess control strategy," *IEEE Transactions on Sustainable Energy*, vol. 8, no. 2, pp. 772–781, 2016, doi.org/10.1109/TSTE.2016.2619759.

[24] R. W. Erickson, D. Maksimović *et al.*, "Fundamentals of power electronics," vol. 2, 2001.

[25] W. Jing, C. H. Lai, W. S. Wong, and M. D. Wong, "A comprehensive study of battery-supercapacitor hybrid energy storage system for standalone pv power system in rural electrification," *Applied energy*, vol. 224, pp. 340–356, 2018, doi.org/10.1016/j.apenergy.2018.04.106.

[26] A. C. Raveendran and U. B. Manthati, "Dynamic power sharing assisted hybrid controller for pv fed isolated dc microgrid," *IEEE Systems Journal*, vol. 17, no. 1, pp. 1087–1097, 2022, doi.org/10.1109/JSYST.2022.3195812.



Siddhartha Bomma received the B.Tech. degree in Electrical and Electronics Engineering from SR University ,Warangal,India, and the M.Tech. degree in Power Electronics and Systems from University college of engineering, Osmania University, Hyderabad, India. He is currently working towards the Ph.D. degree in Hybrid energy storage systems and Bidirectional converters in Electrical Engineering Department, National Institute of Technology, Warangal, India. His research interests include power elec tronic Converters, Energy storage systems.



Udaya Bhasker Manthati received the B.Tech. degree in electrical & electronics engineering and the M.E. degree in power electronics & drives in 2003 and 2006, respectively, and the Ph.D. degree in electrical engineering from the Technical University of Catalonia, Barcelona, Spain, in 2011. Since 2022, he has been an Associate Professor with the Department of Electrical Engineering, National Institute of Technology-Warangal (NIT-W), Warangal, India. During 2011–2022, he was an Assistant Professor with Manipal University Jaipur, Jaipur, India, and NIT-W. During 2007–2011, he was a Research Assistant with CITCEA-UPC, Spain. He has authored and co-authored several papers published in reputed national and international journals and conferences. His research interests include DC-DC converters, power electronics applications to micro grid and smart grid technologies, energy storage systems, digital control, and synchrotron power supplies. He was the recipient of the Synchrotron Light Laboratory-UPC Fellowship during 2007–2010 and Deutschen Akademischen Austauschdienstes (DAAD) stipend from FH-Deggendorf, Germany in the year 2007. He has successfully supervised two Ph.D. scholars who have been awarded their Ph.D. degrees, while three Ph.D. scholars are currently pursuing their research under his supervision. So far 15 FDP's are organized in electrical engineering applications. He has written two book chapters of international repute. He is currently supervising M.Tech. and Ph.D. thesis in the domain of hybrid energy storage systems and digital control.